*Advanced Materials Interfaces*

ADVANCED MATERIALS INTERFACES Open Access

www.advmatinterfaces.de

RESEARCH ARTICLE OPEN ACCESS

Editor's Choice

# Understanding the Dynamics of Nanoparticle Formation and Evolution in Functional Oxides via In Situ SAXS/WAXS

Elena Vicente[1] | Sylvio Haas[2] | Jose Manuel Serra[1] | María Balaguer[1] | Cecilia Solís[3]

[1]Instituto de Tecnología Química, Universitat Politècnica de València, Consejo Superior de Investigaciones Científicas, Valencia, Spain | [2]Deutsches Elektronen Synchrotron (DESY), Hamburg, Germany | [3]German Engineering Materials Science Center (GEMS) at Heinz Maier-Leibnitz Zentrum, Helmholtz-Zentrum Hereon, Garching, Germany

**Correspondence:** María Balaguer (mabara@itq.upv.es) | Cecilia Solís (cecilia.solis@hereon.de)

**Received:** 29 August 2025 | **Revised:** 4 November 2025 | **Accepted:** 11 November 2025

**Keywords:** electrocatalyst | exsolution | in situ SAXS/WAXS | nanoparticle | perovskite

## ABSTRACT

The formation and evolution of nanoparticles on the surface of oxide catalysts are essential for determining their catalytic performance. Establishing a direct relationship between structure and function requires real-time in situ characterization under operational conditions. Multiple techniques can be used to create catalytically active nanoparticles on catalyst surfaces, including traditional deposition or infiltration methods and novel techniques such as exsolution, which allows the in situ growth of stable particles. In this study, we report the first in situ Small-Angle and Wide-Angle X-ray Scattering (SAXS/WAXS) investigation of Ni nanoparticle formation in $La_{0.85}Sr_{0.15}Cr_{0.8}Ni_{0.2}O_{3-\delta}$ (LSCN), where particles emerge via exsolution, and in a reference $La_{0.85}Sr_{0.15}CrO_{3-\delta}$ sample with infiltrated Ni (LSC+5N), at synchrotron facilities. The results reveal early nucleation and thermal evolution with high sensitivity and statistical robustness. By tracking nanoparticle formation and evolution during reduction at increasing temperatures, SAXS provides a complementary tool to conventional techniques such as XRD and electron microscopy for real-time monitoring. This study establishes SAXS/WAXS as a powerful and innovative tool for investigating nanoscale processes in functional ceramic materials, offering new insights into the design of stable and active nanostructured catalysts.

## 1 | Introduction

In heterogeneous catalysis and electrocatalysis, the surface of the catalyst is crucial for determining its catalytic activity, selectivity, and stability. The surface of the catalyst hosts the active sites where the reactants adsorb, transform through a reaction, and desorb as products [1]. Besides compositional surface characteristics, such as chemical composition, electronic structure, coordination environment, and metal-support interaction, morphological factors such as surface area and porosity affect the catalyst performance and reaction kinetics [2]. Deactivation mechanisms such as poisoning or sintering under operating conditions can affect the long-term utility and stability of the catalyst. Therefore, optimizing the surface properties through tailor-made synthesis, structural modifications, promoter addition, and nano catalyst size stability may enhance catalyst kinetics, selectivity and durability.

The most commonly used techniques to disperse a catalyst onto a support surface are wet or dry impregnation, in which the support is soaked in a solution containing the catalyst precursor or a controlled amount of solution is added (Incipient Wetness Impregnation), respectively. Techniques such as precipitation or co-precipitation involve the precipitation of the catalyst precursor from a solution onto the support or simultaneously with the support, ensuring strong interactions [3]. Deposition techniques, such as Chemical Vapor Deposition (CVD) [4], Electrochemical Deposition (ED), and Atomic Layer Deposition (ALD) [5] are

advanced methods for the selective and controllable attachment of catalysts onto the support surfaces. In contrast to conventional methods, the ex-solution process enables a more uniform dispersion of nanoparticles and improved control over their size. In exsolved systems, nanoparticles are strongly embedded in the oxide substrate, solving the problem of weak adhesion between the support and the deposited or infiltrated nanoparticles, which often produce inactivation problems such as agglomeration and poisoning [6–8].

In addition to chemical composition, the catalytic properties of the nanoparticles are determined by their shape, size, and concentration [9]. Characterizing and correlating performance/morphology relationships involves a combination of structural, spectroscopic, and in situ techniques, when possible. The most commonly used method is Transmission Electron Microscopy (TEM), which can provide a direct image of the shape and size of the nanoparticles. In the High-Resolution variant (HRTEM), it is also possible to identify lattice facets and crystallinity. Scanning Electron Microscopy (SEM) is also useful for characterizing the surface morphology of larger particles. Moreover, other techniques are used to determine the compositional features and oxidation states of the active sites, such as Low-Energy Ion Scattering (LEIS), Auger electron spectroscopy (AES), and X-ray Photoelectron Spectroscopy (XPS) [10, 11]. However, these techniques characterize the evolution process by focusing on resolution at the cost of analyzing small sample volumes.

Conversely, Small Angle X-ray Scattering (SAXS) is a valuable technique for the in situ characterization of nanoparticle formation and evolution under different conditions. It overcomes the instrumental limitations of the crystallinity necessity of X-Ray Diffraction (XRD) and the reduced statistical significance of electron microscopy, with the advantage of providing information about changes in size, shape, and volume % [12, 13]. Overall, it provides a much larger volume % analysis than conventional structural characterization techniques such as scanning and transmission electron microscopy.

In situ SAXS has been employed to monitor the evolution and agglomeration-related degradation of different nano catalysts under working conditions [14–16]. Impregnated nanocatalysts have been widely studied using both ex situ [17–20] and in situ SAXS [21–23]. However, to date, SAXS has only been used for the ex situ analysis of exsolved nanoparticles in nanoporous and sintered $La_{0.52}Sr_{0.28}Ti_{0.94}Ni_{0.06}O_{3\pm\delta}$ [10] and in $PrBaCo_2O_{6-\delta}$ double perovskites [24]. To the best of our knowledge, there are currently no references to in situ SAXS monitoring of the exsolution process. Instead, in situ characterization of exsolution has primarily been carried out using in situ TEM, XPS, X-Ray Absorption Near Edge Structure (XANES), XRD and Neutron Diffraction (ND) [25–30].

In previous studies, we investigated the influence of the Ni nanocatalyst deposition method on the electrodes of proton-ceramic electrochemical cells [31–33]. Ni has been widely studied in the field of energy conversion and storage devices, such as solid-oxide fuel cells, electrolyzers, and reforming catalysis, particularly for electrodes with high electrochemical activity and long-term stability [34–36]. However, for specific electrolyte compositions, such as lanthanum tungstate-based, the compatibility between Ni and the electrolyte can be compromised, thus affecting the final device performance [32, 37]. For this reason, alternative anode materials need to be used in those cases.

$La_{0.85}Sr_{0.15}CrO_{3-\delta}$ (LSC)-based materials have been studied as $H_2$-electrode materials for high-temperature fuel cells and electrolyzers [38–40]. Besides, LSC can host cations (such as Ce, Ni, Mn, Fe, and Co) to be exsolved in situ on their surface to enhance the electrocatalytic activity [41–43]. Our previous studies on $La_{5.6}WO_{11.4-\delta}$ (LWO) protonic electrolytes demonstrated that the best anode performance was obtained for LSC material, both doped and infiltrated with Ni [29]. Although the materials have been thoroughly investigated from an electrochemical perspective, no structural analysis has been conducted on the formation and evolution of the resulting Ni nanoparticles.

The main objective of this study is to demonstrate the strength of the in situ SAXS technique in characterizing the evolution of the morphology and size of surface nanoparticles. SAXS offers fast and precise monitoring of the nanoparticles under operating conditions. In particular, this study monitored the high-temperature evolution of Ni nanoparticles on chromite through in situ SAXS/WAXS synchrotron measurements. In addition, the study compares the behavior of nanoparticles obtained by infiltration (LSC sample infiltrated with Ni, LSC+5N) with those obtained by exsolution in Ni-doped chromite ($La_{0.85}Sr_{0.15}Cr_{0.8}Ni_{0.2}O_{3-\delta}$, LSCN) under high-temperature reducing conditions. To unambiguously correlate the microstructural observations with the presence of the nanoparticles, a $La_{0.85}Sr_{0.15}CrO_{3-\delta}$ (LSC) reference sample was also studied.

## 2 | Results and Discussion

High-energy synchrotron X-ray diffraction (SXRD) enabled the identification of the constituent phases in all the as-prepared samples (Figure 1 with different expected crystal structures). All samples predominantly consisted of orthorhombic *Pnma* $La_{0.85}Sr_{0.15}CrO_3$ perovskite (ICSD 51197, marked with green * in Figure 1a) together with some minor monoclinic *P121/n1* $SrCrO_4$ (ICSD 40922, marked with magenta 0 in Figure 1a). The LSC+5N sample also shows expected Bragg reflections corresponding to the infiltrated NiO phase (see inset of Figure 1a), which are significantly broadened, corresponding to a crystallite size of 15 nm from peak width analysis. The wt.% and lattice parameter of the constituting phases obtained from the Rietveld refinements (Figure S1) are summarized in Table 1.

The change in the surface caused by NiO-infiltrated nanoparticles and the exsolution of Ni upon reduction at 900°C in 5% $H_2$ were investigated by microscopy before and after the thermal treatment. The as prepared LSC, LSC+5N, and LSCN samples exhibited similar perovskite grain sizes (SEM images in Figure 2a–c, respectively). In LSC and LSCN, a very low vol% of nanoparticles inherent to the support was observed. The LSC+5N sample presented a significantly higher volume % of nanoparticles corresponding to the infiltrated NiO (Figures S2 and S3) with 17 ± 7 nm in average size, in good agreement with the value obtained from SXRD (Table 1).

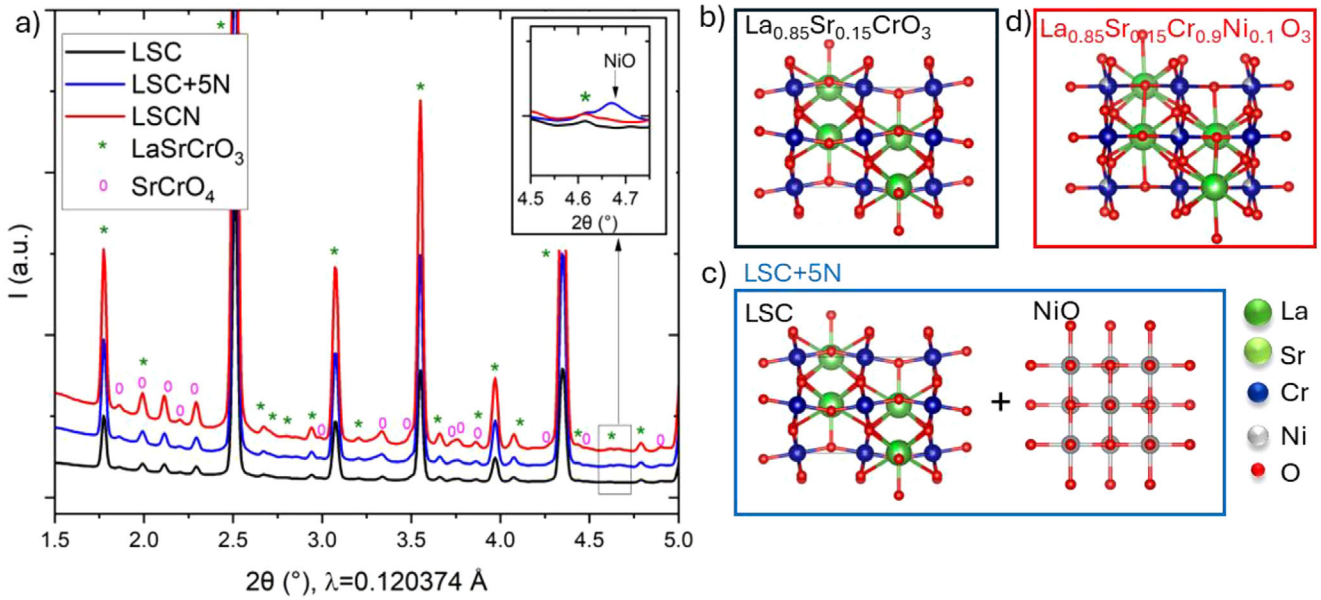


**FIGURE 1** | (a) SXRD patterns of as prepared samples. Green * represent Bragg reflections of *Pnma* $La_{0.85}Sr_{0.15}CrO_3$ perovskite phase and magenta 0 are the *P121/n1* $SrCrO_4$ phase. The inset zooms in the presence of NiO in the LSC+5N sample. (b) Crystal structure of $La_{0.85}Sr_{0.15}CrO_3$ perovskite, (c) together with NiO and d) doped $La_{0.85}Sr_{0.15}Cr_{0.9}Ni_{0.1}O_3$.

**TABLE 1** | Phases, wt.%, and lattice parameters and crystallite sizes obtained from Rietveld refinement of the SXRD of the as-prepared powders measured at RT.

| Phase | wt.% | *a* (Å) | *b* (Å) | *c* (Å) | *α=β; β* (°) | Size (Å) |
|---|---|---|---|---|---|---|
| **As-sintered LSC** | | | | | | |
| *Pnma* $La_{0.85}Sr_{0.15}CrO_3$ | 91.3(3) | 5.4750(5) | 7.7560(6) | 5.5184(4) | 90;90 | |
| *P121/n1* $SrCrO_4$ | 8.7(4) | 7.095(6) | 7.393(5) | 6.761(5) | 90; 103.13(7) | |
| **As-sintered LSC+5N** | | | | | | |
| *Pnma* $La_{0.85}Sr_{0.15}CrO_3$ | 90(3) | 5.4745(5) | 7.7574(7) | 5.5181(4) | 90;90 | |
| *P121/n1* $SrCrO_4$ | 6.6(4) | 7.094(9) | 7.389(7) | 6.759(7) | 90; 103.09(11) | |
| *Fm-3m* NiO | 3.4(4) | 4.178(3) | 4.178(3) | 4.178(3) | 90;90 | 147(2) |
| **As-sintered LSCN** | | | | | | |
| *Pnma* $La_{0.85}Sr_{0.15}CrO_3$ | 89(2) | 5.4756(4) | 7.7598(5) | 5.5206(3) | 90;90 | |
| *P121/n1* $SrCrO_4$ | 10.6(3) | 7.101(4) | 7.396(3) | 6.770(3) | 90; 103.12(4) | |

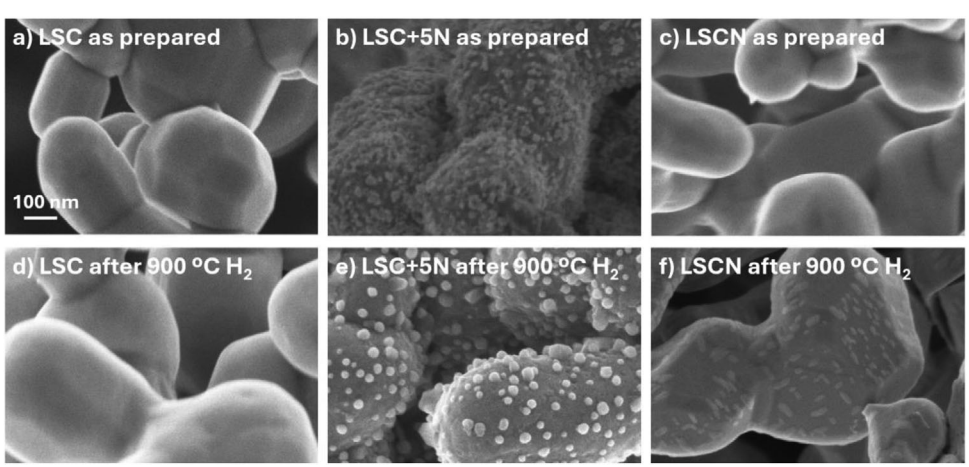


**FIGURE 2** | (a–c) SEM images of LSC, LSC+5N, and LSC powders as sintered and (d–f) after heat treatment up to 900°C in 5% of $H_2$ in Ar.

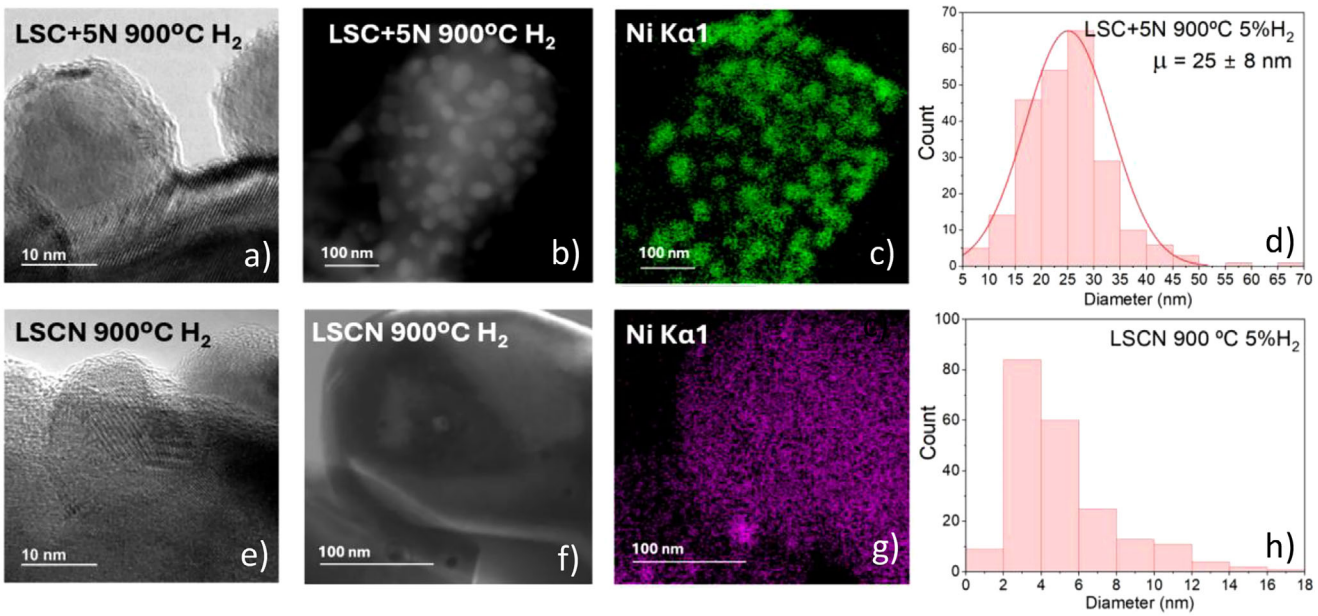


**FIGURE 3** | (a,b) HR-TEM electron images, c) EDX spectrum of the Ni K$\alpha$ X-ray line, and d) Ni particle size histogram of LSC+5N. (e,f) HR-TEM electron images, g) EDX spectrum of the Ni K$\alpha$ X-ray line, and h) Ni particle size histogram of LSCN after heating up to 900°C in 5% of $H_2$ in Ar.

After exposing the samples to 900°C in 5%$H_2$ for 1.5 h (Figure 3d–f), no difference was detected in the LSC structure, and the same grain and nanoparticle sizes as those shown in the as-prepared sample were observed. In the LSC+5N sample, NiO particles were reduced to metallic Ni and grew to an average size of 25 ± 8 nm, as confirmed by SEM and HRTEM-EDX (Figures 2e and 3a–d). The interplanar distances measured via Digital Diffraction Pattern (DPP) analysis further confirmed the phases of the supported Ni nanoparticles (Figure S4). For LSCN, an additional phase/microstructure was observed on the surface, identified as SrO by HRTEM-EDX (Figure S5) and WAXS (as will be shown later), coexisting with metallic Ni nanoparticles. The Ni composition of these nanoparticles was confirmed by EDX (Figure 3e–h), and the obtained grain size ranges were mainly between 2 and 6 nm, as can be inferred from the grain size distribution. The interplanar distances of the three constituent phases also correlated with the measured d-spacings in their respective DDPs (Figure S6).

The evolution of the infiltrated NiO nanoparticles and the Ni exsolution process in the doped material were monitored during reduction at high temperatures using in situ SAXS/WAXS measurements. In addition, the LSC reference material was studied under similar heat treatment to identify any contribution of the base material and unambiguously ascribe changes in the scattering signal to the presence or changes in the nanoparticles.

During the heating step in reducing atmospheres, the orthorhombic perovskite phase transformed into rhombohedral (ICSD 51193) at approximately 225°C, in agreement with other studies [44]. This can be easily inferred from the splitting of the peak at q = 22.6 $nm^{-1}$ in the WAXS patterns for the LSCN sample (Figure 4a). The Rietveld refinement of LSCN at 400°C (Figure 4b) shows the double peak characteristic of the rhombohedral structure at ~2q = 21.5 ° (see Figure S7, the Rietveld refinement at RT for comparison). At higher temperatures (>800°C), independent Bragg reflections began to combine, which could be an indication of a further transformation into a cubic phase (reported to take place above 1000°C) [42]. Besides, at higher temperatures, the $SrCrO_4$ phase disappeared (above 825°C).

From the Rietveld refinement at 900°C (Figure 4c), it can be seen the presence of $LaCrO_3$ rhombohedral structure (84.6 + 0.7 wt.%) together with some remaining orthorhombic phase (3.0 ± 0.7 wt.%), but also SrO (9 ± 1 wt.%) and metallic Ni (3.4 ± wt.%). This proves the Ni exsolution in the doped compound at high temperatures, which occurs together with the exsolution of some SrO-related nanostructure (secondary phase observed in Figure 2f). Metallic Ni was also observed after reducing the NiO present in sample LSC+5N at RT (see Figure S8, the Rietveld refinements of WAXS patterns of LSC and LSC+5N at 900°C).

To properly monitor the sizes and morphology of the nanoparticles, SAXS measurements during heating were simultaneously performed with WAXS (Figure 5a–c for LSC reference material, LSC+5N, and LSCN). The temperature evolution of the scattering curves showed clear differences among the three samples (highlighted with arrows in Figure 5b,c). Thus, a proper analysis was performed by fitting the data to spherical nanoparticles with a lognormal size distribution. The temperature evolution of the obtained sizes (mean diameter of the spheres) and volume % of the nanoparticles can be seen in Figure 5d–f, and the corresponding size distribution at RT and at 900°C in Figure 5g–i for LSC reference, LSC+5N, and LSCN samples, respectively.

The LSC reference sample showed a volume of less than 0.5% of very small nanoparticles (4 nm), which remain constant in the whole temperature range (Figure 5d). These small particles are consistent with those observed by SEM, and although their exact nature remains unclear,

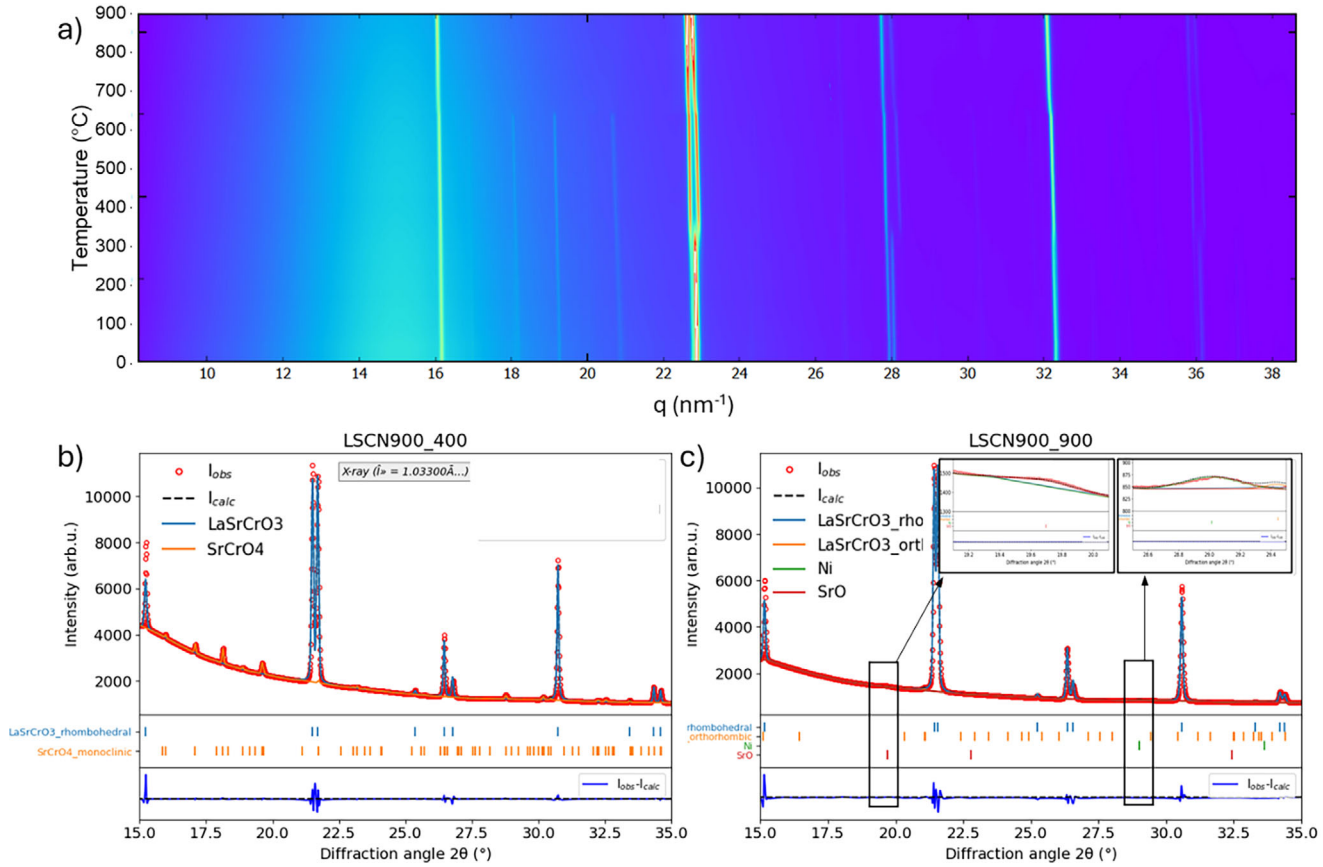


**FIGURE 4** | (a) WAXS diffraction patterns of LSCN during heating up to 900°C in reducing atmosphere, (b) Rietveld refinement at RT and (c) 900°C, with zooms from 19.1 to 20.1 and from 28.5 to 29.5°, where the SrO and Ni Bragg reflections are observed.

they are considered intrinsic to the studied perovskite material.

The large number of NiO nanoparticles observed by SEM in the LSC+5N sample could also be detected by SAXS at RT (Figure 5e). The proper modelling of these SAXS data requires the use of two families of precipitates. The smaller ones, with a mean size of 4 nm and 6 vol.% at RT, are very stable in size but present a much broader size distribution than those observed in the LSC reference sample (solid lines in Figure 5g,h). In addition, they decreased in volume % above 600°C. The second family of precipitates, of 14 nm and 3 vol.% at RT, increases in size and vol.% from 600°C, reaching 20 nm and 11 vol.% at 900°C. This behavior can be correlated with the reduction and coarsening of the larger precipitates, in this case at the expense of the smaller ones, following an Ostwald ripening process, as already observed in other Ni nanoparticles [45]. It is important to emphasize that SAXS enables the in situ evaluation of two different families of nanoparticles simultaneously, which cannot be easily distinguished using SEM. In contrast, the smaller sizes obtained from SAXS compared to SEM likely reflect the inherent difference in statistical weighting, with SEM providing area-weighted dimensions, whereas SAXS yields volume-weighted size distributions [11].

The LSCN sample at RT (Figure 5f) shows very small precipitates (<5 nm) in a fraction below 0.5 vol.%. The behavior of these precipitates was similar to that shown by the reference LSC sample up to 600°C (with no changes in size and volume %) and therefore can be considered inherent to the perovskite behavior (Figure 5d). Above 600°C, the nanoparticles increased in size up to 6.5 nm at 900°C, but maintained a narrow size distribution, and in volume % up to 2 vol.%, that is more than a fourfold rise (Figure 5i). Besides, from 600°C, a second family of nanoparticles appears, with 3 vol.% and mean sizes ranging from 2 to 2.5 nm from 600 to 900°C. Both families of nanoparticles that nucleated above 600°C were unambiguously ascribed to the metallic Ni measured by WAXS and observed by SEM (Figure 2f) and TEM (Figure 3d–f) with reasonable agreement in size distribution.

SAXS analysis permitted the identification of the starting temperature of the exsolution process, 600°C in the LSCN sample, and enabled a precise examination of the size evolution. Exsolved nanoparticles remained smaller and with narrower size distributions than nanoparticles obtained from infiltration after reduction (with up to four times difference at 900°C), which is a characteristic of the properly embedded exsolved nanoparticles compared to those infiltrated.

To elucidate the catalyst-surface differences arising from the unique anchoring of exsolved nanoparticles compared to infiltrated ones, in situ SAXS measurements were performed on both samples, i.e., LSC+5N and LSCN, over 90 min at 900°C (see SAXS curves in Figure S9). The corresponding particle size and volume % evolutions are depicted in Figure 6a,b for LSC+5N and

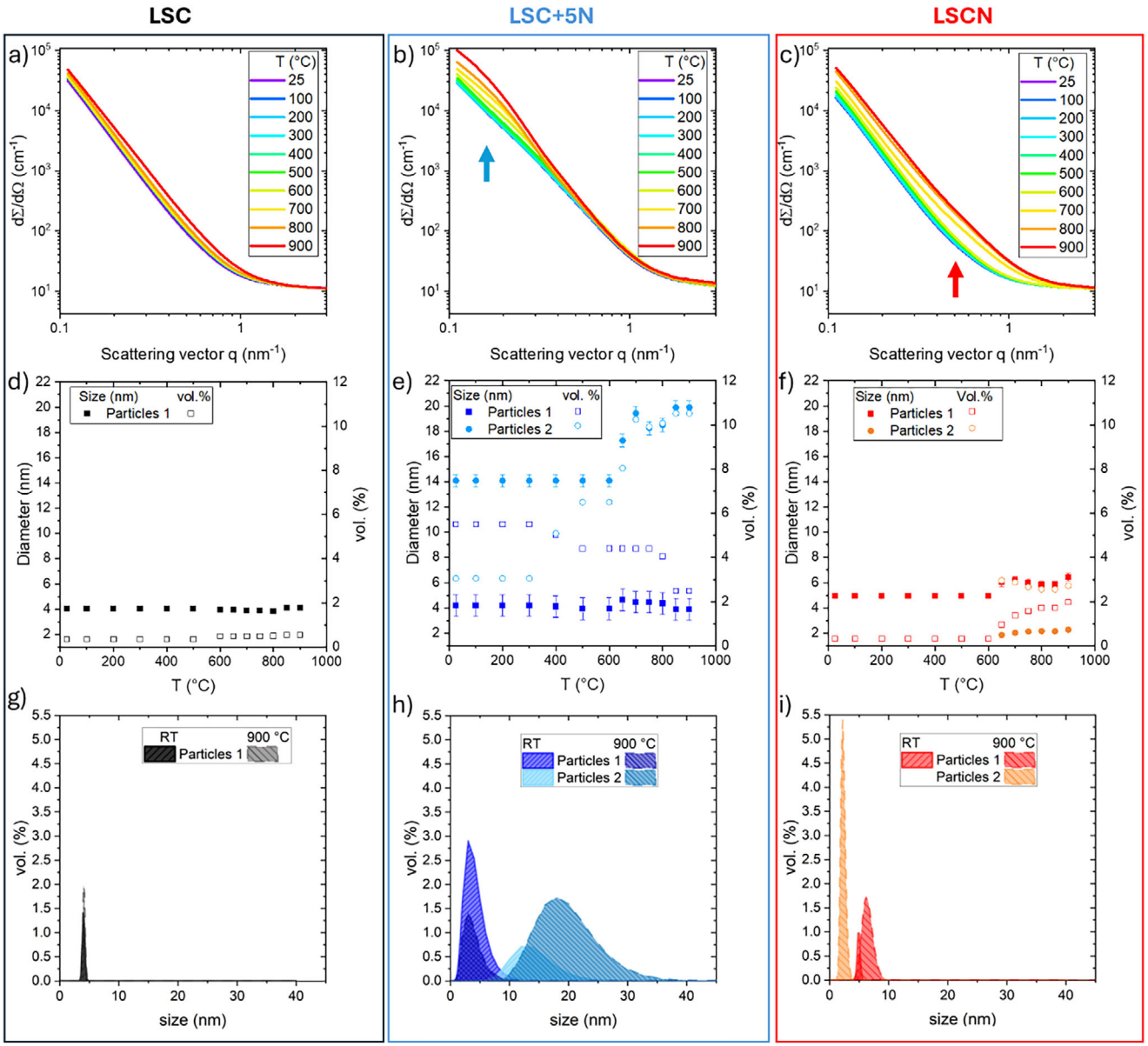


**FIGURE 5** | (a–c) SAXS curves during heating from RT up to 900°C in 5%$H_2$ in Ar, where arrows indicate main changes, (d–f) average diameter and vol.% of obtained spherical particles as a function of temperature and (g–i) log-normal size distribution at room temperature and 900°C for LSC, LSC+5N and LSCN samples.

LSCN, respectively. In both cases, the particle volume % remains nearly constant (or slightly decreases) across all particle families, suggesting that nucleation has ceased.

Distinct behaviors were observed in the size evolution over time. For the Ni-infiltrated sample (LSC+5N), both families of particles grew continuously (from 4 to 11 nm and 20 to 23 nm after 90 min) following a well-established diffusion-controlled Ostwald ripening mechanism described by [45]:

$$r^3 = r_0^3 + Kt \tag{1}$$

where $r$ is the radius of the nanoparticle at time $t$, $r_0$ is the particle size at the start of coarsening and $K$ is the growth coefficient. The fitted values indicate comparable coarsening kinetics for both particle families, with growth coefficients of $K = 0.022 \pm 0.004$ $nm^3/s$ for the smaller particles and $K = 0.020 \pm 0.008$ $nm^3/s$ for the larger ones.

In contrast, the exsolved nanoparticles in LSCN, which are strongly anchored to the oxide surface, show negligible growth, i.e., the $K$ value is almost 0. Only a slight broadening of the size distribution was observed for the larger particles (reflected in increasing error bars), likely due to the partial dissolution of smaller particles, consistent with recent reports [43]. It should be noted that Ostwald ripening of exsolved nanoparticles was recently reported by Jennings et al. [45]. In their study, the coarsening was evaluated starting after the exsolution process. In our case, we analyzed the size evolution of the precipitates at 900°C, whereas exsolution started at 600°C. Consequently, any coarsening occurred during heating from 600 to 900°C

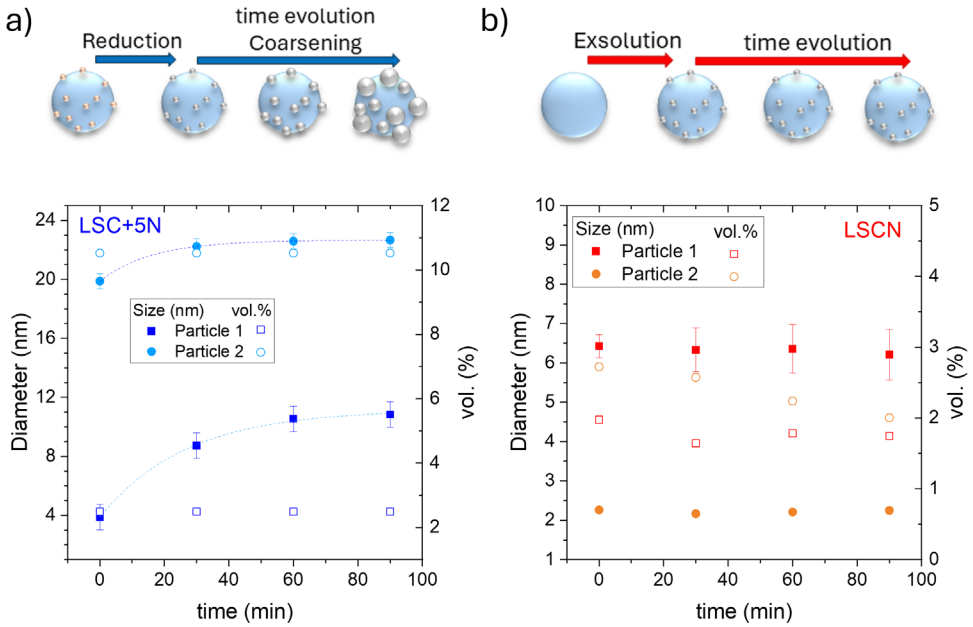


**FIGURE 6** | (a) Size evolution as a function of time at 900°C for LSC+5N and (b) LSCN. Lines correspond to fits of the diffusion-controlled ripening model (Equation 1). The first data point for the larger precipitates was excluded, as it deviated from the overall trend, probably influenced by growth at lower temperatures.

(Figure 5f), after which the particle sizes remained essentially stable.

In summary, the SAXS/WAXS method provides detailed information on the surface morphology of the catalyst particles and their evolution under gas and temperature operating conditions. When combined with complementary characterization techniques such as SEM/TEM and catalytic performance data, it enables the rational design of improved catalysts. Notably, exsolved nanoparticles exhibit high stability and limiting coarsening at high temperatures. However, under the conditions described in this study, their formation remains suboptimal as addressed in [29]. Through an additional infiltration step, it was demonstrated that the catalytic performance of the anode was further improved, and agglomeration did not readily occur under the studied conditions [29, 30]. By understanding the nucleation temperature and growth kinetics, it is possible to design catalysts that leverage the advantages of each approach.

## 3 | Conclusions

In situ SAXS/WAXS experiments have proven to be a powerful and versatile technique for elucidating the reduction dynamics and nanoparticle growth of infiltrated catalysts, as well as for tracking the exsolution process of Ni-doped perovskite under reducing environments at high temperatures. The high time resolution enables detailed observation of distinct processes, such as nucleation, growth, and coarsening, while the larger sample volume analyzed compared to microscopy techniques ensures statistically robust insights that better represent the true bulk behavior of materials. SAXS provides a direct determination of the temperature at which the first Ni nanoparticles are exsolved, regardless of their crystallinity, and enables the characterization of the high-temperature evolution of the nanoparticles over time. This allows for the distinction between the growth and coarsening of infiltrated Ni nanoparticles and the anchoring behavior of exsolved Ni nanoparticles, while quantifying the number and size distribution of the formed nanoparticles.

Beyond Ni-based systems, this combined SAXS/WAXS methodology can be readily extended to other surface chemistries, with particular interest in exsolution such as Co-, Fe-, or Cu-based perovskites, metal alloy nanoparticles or even to multi-component systems where simultaneous metal exsolution and oxide restructuring occur. Moreover, its compatibility with operando conditions makes it a valuable tool for probing the dynamic structural and morphological changes in functional catalysts during real electrochemical, redox, or thermal reaction environments. Such insights are critical for correlating nanoscale evolution with macroscopic catalytic or electrochemical performance, thereby guiding the rational design of more stable and active catalysts for a wide range of energy conversion and storage applications.

## 4 | Materials and Methods

### 4.1 | Materials Preparation

The citrate reaction route was used to prepare $La_{0.85}Sr_{0.15}CrO_{3-\delta}$ (LSC) and $La_{0.85}Sr_{0.15}Cr_{0.8}Ni_{0.2}O_{3-\delta}$ (LSCN) powders, as described elsewhere [46, 47]. Stoichiometric amounts of the corresponding metal nitrates were dissolved together in the minimum amount of water at 60°C. The metals were complexed with a solution of citric acid solution with a citrate-to-cation molar ratio of 2. Crosslinking (polyesterification) of the citrate complexes was boosted by adding ethylene glycol at an ethylene glycol-to-cation molar ratio of 4 and heating the solution at 100°C under vigorous stirring. The resulting gel was dried at 220°C overnight at later

**TABLE 2** | Summary of sample acronyms, compositions and sintering and reducing treatments undergone.

| Acronym | Composition | Sintering treatment | Reducing treatment |
|---|---|---|---|
| LSC | $La_{0.85}Sr_{0.15}CrO_{3-\delta}$ | 900°C for 12 h in air | – |
| LSC $H_2$ 900°C | $La_{0.85}Sr_{0.15}CrO_{3-\delta}$ | 900°C for 12 h in air | 900°C for 1.5 h in 5%$H_2$/Ar |
| LSCN | $La_{0.85}Sr_{0.15}Cr_{0.8}Ni_{0.2}O_{3-\delta}$ | 900°C for 12 h in air | – |
| LSCN $H_2$ 900°C | $La_{0.85}Sr_{0.15}Cr_{0.8}Ni_{0.2}O_{3-\delta}$ | 900°C for 12 h in air | 900°C for 1.5 h in 5%$H_2$/Ar |
| LSC+5N | 5%wt.Ni/$La_{0.85}Sr_{0.15}CrO_{3-\delta}$ | 900°C for 12 h in air (LSC) + 450°C for 6 h in air (after infiltration) | – |
| LSC+5N $H_2$ 900°C | 5%wt.Ni/$La_{0.85}Sr_{0.15}CrO_{3-\delta}$ | 900°C for 12 h in air (LSC) + 450°C for 6 h in air (after infiltration) | 900°C for 1.5 h in 5%$H_2$/Ar |

sintered at 900°C for 12 h. A portion of the LSC powder (2 g) was infiltrated with Ni using an aqueous solution of nickel nitrate (208 mg of $Ni(NO_3)_2{\cdot}6H_2O$, Sigma–Aldrich) dissolved in 1.5 mL of deionized water, which reached a loading of 5 wt.% Ni (denoted as LSC + 5N). The impregnated powder was then calcined at 450°C for 6 h to decompose the nitrates. The prepared materials were later subjected to a reducing treatment with 5% $H_2$/Ar for 1.5 h at 900°C (20°C·min$^{-1}$ of heating rate) for electron microscopy characterization. Table 2 presents a summary of all the studied samples, including their composition, sintering and reducing treatments:

## 4.2 | Structure Characterization

The phase compositions of the as-received and reduced materials were characterized by Laboratory X-Ray Diffraction (XRD) using a PANalytical Cubix diffractometer with CuK$\alpha_{1,2}$ radiation and an X'Celerator detector in Bragg–Brentano geometry. XRD patterns were recorded in the 2$\theta$ range of 10°–90° and analyzed using X'Pert Highscore Plus software. Synchrotron X-Ray Diffraction (SXRD) measurements of the pristine materials were obtained at the High Energy Materials Science (HEMS) [48] beamline at PETRA III at DESY using a photon energy of 103 keV ($\lambda$ = 0.1204 Å). The 2D patterns from the synchrotron measurements were treated with the software pyDIDAS (python Diffraction Data Analysis Suite) [49], and Rietveld refinement [50] of the obtained diffraction patterns was performed using the FullProf software [51].

The microstructure was investigated using Scanning Electron Microscopy (SEM) (Zeiss Ultra 55), and elemental analysis was carried out with Energy-Dispersive X-ray Spectroscopy (EDS) (INCA, Oxford). Particle size distribution for each reduced sample was obtained with its statistical parameters (the $\pm\sigma$ value). In all cases, a minimum number of 100 particles was considered. This study was performed using an image analyzer software (ImageJ).

For higher magnifications, High-Resolution Transmission Electron Microscopy (HR-TEM) images were collected on a 200 kV Jeol JEM-2100F instrument running in a Scanning Transmission Electron Microscopy (STEM) mode. Elemental analysis was performed using an Energy-Dispersive X-ray Spectroscopy (EDX) X-Max 80 detector with a resolution of 127 eV. To calculate interplanar distances out of TEM micrographs, ImageJ software was also employed in order to obtain Fast Fourier Transform (FFT) and inverse FFT images.

In situ Small Angle X-ray Scattering (SAXS) and Wide-Angle X-ray Scattering (WAXS) were performed at the SAXSMAT beamline P62 of PETRA III at DESY, Hamburg (Germany) [52]. For the in situ experiments, the powders were mounted in quartz capillaries (1 mm of outside diameter and 0.01 mm of wall thickness), placed on a heater, and then monochromatically irradiated with X-rays at an energy of 12 keV ($\lambda$ = 1.0332 Å). For all measurements, we used a 400x400 µm spot size and a Q range from 0.11 to 7 nm$^{-1}$ for SAXS and 8.3 to 38 nm$^{-1}$ for WAXS. $AgO_2C(CH_2)_{20}CH_3$ and Si powder samples were measured to determine the SAXS and WAXS detector parameters. The LSC, LSCN and LSC+5N samples were continuously monitored (measurements taken every 5 s) from room temperature (RT) to 900°C under a 5%$H_2$/Ar atmosphere with a heating rate of 20°C·min$^{-1}$. Afterward, SAXS/WAXS measurements were taken under constant conditions at 900°C under a 5%$H_2$/Ar atmosphere for 90 min. SAXS data analysis was performed considering background and empty capillary corrections and using a pre-calibrated glassy carbon sample for the scaling intensities to absolute differential scattering cross section.

For the analysis of the SAXS data analysis, the differential scattering cross section was fitted using a model to obtain information on the particle shape, size, size distribution, and volume fraction. The absolute differential scattering cross section of the material is defined as

$$\frac{\partial \Sigma(q)}{\partial \Omega} = NV^2(\Delta\rho)^2 P(q) S(q) + B$$

where $N$ is the number of nanoparticles per unit of volume, $V$ is the volume of each nanoparticle, $\Delta\rho$ is the scattering contrast (difference in the scattering length densities of the nanoparticles and surrounding material, $\Delta\rho = \rho_m - \rho_{np} = \sum_{i=1}^{M} \frac{x_i^m b_i}{v_m} - \sum_{j=1}^{N} \frac{x_j^n b_j}{v_n}$), $P(q)$ is the particle form factor, $S(q)$ is the structure factor, and $B$ is the background corresponding to the additional incoherent scattering contribution and diffuse scattering [53].

As the volume fraction determination from SAXS strongly depends on the scattering contrast, $\Delta\rho$ which depends on the chemical composition of the nanoparticles and surrounding material, relative units are used for the volume %

determination, assuming always the same scattering contrast (no changes in composition of both precipitates and surrounding material regardless of the heat treatment).

The SASFit software [54] was used to analyze the SAXS data assuming the form factor of spherical particles with a lognormal particle size distribution. The size data obtained from SAXS and shown in the graphs correspond to the mean diameter value obtained from the lognormal size distribution. FullProf software was used to analyze the WAXS data.


### Acknowledgements

The authors acknowledge DESY (Hamburg, Germany), a member of the Helmholtz Association HGF, for providing experimental facilities. SAXS-WAXS measurements were performed at P62 (beamtime allocated for proposal I-20240066 EC) and high energy XRD measurements were performed at P07 (Petra III). We also extend our appreciation to the Electron Microscopy Service of the Universitat Politècnica de València and to Ana María García Castillo for her thoughtful help with image editing. Financial support from the Spanish National Research Council (CSIC) through the project PIE 20238AT016 and to the Spanish Government through the CEX2021-001230-S grant funded by MCIN/AEI/10.13039/501100011033, are also acknowledged

Open access funding enabled and organized by Projekt DEAL.


### Conflicts of Interest

The authors declare no conflicts of interest.

### Data Availability Statement

The data that support the findings of this study are available from the corresponding author upon reasonable request.

### References


1. W. Gao, Z. D. Hood, and M. Chi, "Interfaces in Heterogeneous Catalysts: Advancing Mechanistic Understanding Through Atomic-Scale Measurements," *Accounts of Chemical Research* 50 (2017): 787–795, https://doi.org/10.1021/acs.accounts.6b00596.

2. W. Huang and W. X. Li, "Surface and Interface Design for Heterogeneous Catalysis," *Physical Chemistry Chemical Physics* 21 (2019): 523–536, https://doi.org/10.1039/C8CP05717F.

3. B. A. T. Mehrabadi, S. Eskandari, U. Khan, R. D. White, and J. R. Regalbuto, "Chapter One—A Review of Preparation Methods for Supported Metal Catalysts," *Advances in catalysis* 61 (2017): 1–35, https://doi.org/10.1016/bs.acat.2017.10.001.

4. R. Moene, M. Makkee, and J. A. Moulijn, "Chemical Vapour Deposition as a Novel Technique for Catalyst Preparation; Modelling of Active Phase Profiles," *The Chemical Engineering Journal and the Biochemical Engineering Journal* 53 (1993): 13–24, https://doi.org/10.1016/0923-0467(93)80003-F.

5. B. J. O'Neill, D. H. K. Jackson, J. Lee, et al., "Catalyst Design With Atomic Layer Deposition," *ACS Catal* 5 (2015): 1804, https://doi.org/10.1021/cs501862h.

6. Y. H. Kim, H. Jeong, B.-R. Won, et al., "Nanoparticle Exsolution on Perovskite Oxides: Insights Into Mechanism, Characteristics and Novel Strategies," *Nano-Micro Letters* 16 (2024): 33, https://doi.org/10.1007/s40820-023-01258-4.

7. Y. Luo, X. Chang, J. Wang, et al., "Precise Regulation of in Situ Exsolution Components of Nanoparticles for Constructing Active Interfaces Toward Carbon Dioxide Reduction," *ACS Nano* 19 (2025): 1463–1477, https://doi.org/10.1021/acsnano.4c14279.

8. A. J. Carrillo, A. López-García, B. Delgado-Galicia, and J. M. Serra, "New Trends in Nanoparticle Exsolution," *Chemical Communications* 60 (2024): 7987–8007, https://doi.org/10.1039/D4CC01983K.

9. S. Cao, F. F. Tao, Y. Tang, Y. Lia, and J. Yu, "Size- and Shape-dependent Catalytic Performances of Oxidation and Reduction Reactions on Nanocatalysts," *Chemical Society Reviews* 45 (2016): 4747–4765, http://doi.org/10.1039/C6CS00094K.

10. O. Kwon, S. Joo, S. Choi, S. Sengodan, and G. Kim, "Review on Exsolution and Its Driving Forces in Perovskites," *Journal of Physics: Energy* 2 (2020): 032001, https://doi.org/10.1088/2515-7655/ab8c1f.

11. K. Kousi, C. Tang, I. S. Metcalfe, and D. Neagu, "Emergence and Future of Exsolved Materials," *Small* 17 (2021): 2006479, https://doi.org/10.1002/smll.202006479.

12. P. R. A. F. Garcia, O. Prymak, V. Grasmik, et al., "An in Situ SAXS Investigation of the Formation of Silver Nanoparticles and Bimetallic Silver–gold Nanoparticles in Controlled Wet-chemical Reduction Synthesis," *Nanoscale Advances* 2 (2020): 225–238, https://doi.org/10.1039/C9NA00569B.

13. B. Rudolph, A. I. Tsiotsias, B. Ehrhardt, et al., "Nanoparticle Exsolution From Nanoporous Perovskites for Highly Active and Stable Catalysts," *Advanced Science* 10 (2023): 2205890, https://doi.org/10.1002/advs.202205890.

14. M. C. Smith, J. A. Gilbert, J. R. Mawdsley, S. Seifert, and D. J. Myers, "In Situ Small-Angle X-ray Scattering Observation of Pt Catalyst Particle Growth During Potential Cycling," *Journal of the American Chemical Society* 130 (2008): 8112–8113, https://doi.org/10.1021/ja801138t.

15. L. Fang, S. Seifert, R. E. Winans, and T. Li Operando XAS/SAXS, "Guiding Design of Single-Atom and Subnanocluster Catalysts," *Small Methods* 5 (2021): 2001194, https://doi.org/10.1002/smtd.202001194.

16. F. Valle, N. Zuliani, B. Marmiroli, H. Amenitsch, and R. Taccani, "SAXS Analysis of Catalyst Degradation in High Temperature PEM Fuel Cells Subjected to Accelerated Ageing Tests," *Fuel Cells* 14 (2014): 938–944, https://doi.org/10.1002/fuce.201300221.

17. G. Albertini, F. Carsughi, C. Casale, F. Fiori, A. L. Monaca, and M. Musci, "X-ray and Neutron Small-angle Scattering. Investigation of Nanophase Vanadium-titanium Oxide Particles," *Philosophical Magazine B* 68 (1993): 949–955, https://doi.org/10.1080/13642819308217952.

18. F. Boubekr, A. Davidson, S. Casale, and P. Massiani, "Ex-nitrate Co/SBA-15 Catalysts Prepared With Calibrated Silica Grains: Information Given by TPR, TEM, SAXS and WAXS," *Microporous and mesoporous materials* 141 (2011): 157–166, https://doi.org/10.1016/j.micromeso.2010.10.038.

19. L. Zhang, J. Yang, J. Zhu, et al., "Properties and Liquefaction Activities of Ferrous Sulfate Based Catalyst Impregnated on Two Chinese Bituminous Coals," *Fuel* 81 (2002): 951–958, https://doi.org/10.1016/S0016-2361(02)00008-X.

20. C.-S. Tsao, Y.-R. Tzeng, M.-S. Yu, et al., "Effect of Catalyst Size on Hydrogen Storage Capacity of Pt-Impregnated Active Carbon via Spillover," *The Journal of Physical Chemistry Letters* 1 (2010): 1060–1063, https://doi.org/10.1021/jz100149u.

21. H. Brumberger, D. Hagrman, J. Goodisman, and K. D. Finkelstein, "In Situ Anomalous Small-angle X-ray Scattering From Metal Particles in Supported-metal Catalysts. II. Results," *Journal of Applied Crystallography* 38 (2005): 324–332, https://doi.org/10.1107/S0021889805002165.

22. J. Kehres, J. G. Jakobsen, J. W. Andreasen, et al., "Dynamical Properties of a $Ru/MgAl_2O_4$ Catalyst During Reduction and Dry Methane Reforming," *Journal of Physical Chemistry C* 116 (2012): 21407–21415, https://doi.org/10.1021/jp3069656.

23. C. Yu, S. Koh, J. E. Leisch, M. F. Toney, and P. Strasser, "Size and Composition Distribution Dynamics of Alloy Nanoparticle Electrocatalysts

Probed by Anomalous Small Angle X-ray Scattering (ASAXS)," *Faraday Discuss* 140 (2009): 283–296, https://doi.org/10.1039/B801586D.

24. A. J. Carrillo, M. Balaguer, C. Solís, et al., "Evaluating Oxide Nanoparticle Exsolution on A-site Deficient $PrBaCo_2O_{6-\delta}$ Electrodes," *Journal of Physics: Energy* 7 (2025): 025007, https://doi.org/10.1088/2515-7655/ada8de.

25. Y.-F. Sun, Y.-Q. Zhang, J. Chen, et al., "New Opportunity for in Situ Exsolution of Metallic Nanoparticles on Perovskite Parent," *Nano Letters* 16 (2016): 5303–5309, https://doi.org/10.1021/acs.nanolett.6b02757.

26. M. T. Azcondo, G. Anemone, A. Muñoz-Noval, et al., "Unveiling the Mechanism of Exsolution of Silver Nanoparticles for Decorating Lanthanum Strontium Ferrite," *Inorganic Chemistry* 63 (2024): 24905–24915, https://doi.org/10.1021/acs.inorgchem.4c04413.

27. J. Guo, A. Berenova, and S. J. Skinner, "In Situ Investigation of Ruthenium Doped Lanthanum Nickel Titanium Double Perovskite and Its Exsolution Behaviour," *Nanoscale Advances* 6 (2024): 4394–4406, https://doi.org/10.1039/D4NA00349G.

28. X. Chen, J. Pei, Y. Guo, Y. Ning, and Q. Fu, "In Situ Probing Dynamic Exsolution of Fe 0 From Perovskite Under Graded Potentials," *The Journal of Physical Chemistry Letters* 16 (2025): 2245–2253, https://doi.org/10.1021/acs.jpclett.5c00175.

29. D. Neagu, V. Kyriakou, I.-L. Roiban, et al., "In Situ Observation of Nanoparticle Exsolution From Perovskite Oxides: From Atomic Scale Mechanistic Insight to Nanostructure Tailoring," *ACS Nano* 13 (2019): 12996–13005, https://doi.org/10.1021/acsnano.9b05652.

30. P. Cao, P. Tang, M. F. Bekheet, et al., "Atomic-Scale Insights Into Nickel Exsolution on LaNiO3 Catalysts via in Situ Electron Microscopy," *The Journal of Physical Chemistry C* 126 (2022): 786–796, https://doi.org/10.1021/acs.jpcc.1c09257.

31. M. Balaguer, C. Solís, F. Bozza, N. Bonanos, and J. M. Serra, "High Performance Anodes With Tailored Catalytic Properties for $La_{5.6}WO_{11.4-\delta}$ Based Proton Conducting Fuel Cells," *Journal of Materials Chemistry A* 1, no. 1 (2013): 3004–3007, https://doi.org/10.1039/C3TA01554H.

32. C. Solís, M. Balaguer, F. Bozza, N. Bonanos, and J. M. Serra, "Catalytic surface promotion of highly active $La_{0.85}Sr_{0.15}Cr_{0.8}Ni_{0.2}O_{3-\delta}$ anodes for $La_{5.6}WO_{11.4-\delta}$ based proton conducting fuel cells," *Applied Catalysis B: Environmental* 147 (2014): 203–207, https://doi.org/10.1016/j.apcatb.2013.08.044.

33. C. Solís, L. Navarrete, M. Balaguer, and J. M. Serra, "Development and Understanding of $La_{0.85}Sr_{0.15}Cr_{1-x}Ni_xO_{3-\delta}$ Anodes for $La_{5.6}WO_{11.4-\delta}$-based Proton Conducting Solid Oxide Fuel Cells," *Journal of Power Sources* 258 (2014): 98–107, https://doi.org/10.1016/j.jpowsour.2014.02.015.

34. A. Hauch, R. Küngas, P. Blennow, et al., "Recent Advances in Solid Oxide Cell Technology for Electrolysis," *Science* 370 (2020): 186, https://doi.org/10.1126/science.aba6118.

35. V. Vij, S. Sultan, A. M. Harzandi, et al., "Nickel-Based Electrocatalysts for Energy-Related Applications: Oxygen Reduction, Oxygen Evolution, and Hydrogen Evolution Reactions," *CS Catalysis* 7 (2017): 7196–7225, https://doi.org/10.1021/acscatal.7b01800.

36. H. Yang, S. F. Hung, S. Liu, et al., "Atomically Dispersed Ni(i) as the Active Site for Electrochemical $CO_2$ Reduction," *Nature Energy* 3 (2018): 140–147, https://doi.org/10.1038/s41560-017-0078-8.

37. D. Han, Y. Otani, Y. Noda, T. Onishi, M. Majima, and T. Uda, "Strategy to Improve Phase Compatibility Between Proton Conductive $BaZr_{0.8}Y_{0.2}O_{3-\delta}$ and Nickel Oxide," *RSC Advances* 6 (2016): 19288–19297, https://doi.org/10.1039/C5RA26947D.

38. G. Pudmich, B. A. Boukamp, M. Gonzalez-Cuenca, W. Jungen, W. Zipprich, and F. Tietz, "Chromite/Titanate Based Perovskites for Application as Anodes in Solid Oxide Fuel Cells," *Solid State Ionics* 135 (2000): 433–438, https://doi.org/10.1016/S0167-2738(00)00391-X.

39. C. Solís, V. B. Vert, M. Balaguer, S. Escolástico, S. Roitsch, and J. M. Serra, "Mixed Proton–Electron Conducting Chromite Electrocatalysts as Anode Materials for LWO-Based Solid Oxide Fuel Cells," *ChemSusChem* 5 (2012): 2155–2158, https://doi.org/10.1002/cssc.201200446.

40. M. Riegraf, D. M. Amaya-Dueñas, N. Sata, K. A. Friedrich, and R. Costa, "Performance and Limitations of Nickel-Doped Chromite Anodes in Electrolyte-Supported Solid Oxide Fuel Cells," *ChemSusChem* 14 (2021): 2401–2413, https://doi.org/10.1002/cssc.202100330.

41. V. B. Vert, F. V. Melo, L. Navarrete, and J. M. Serra, "Redox Stability and Electrochemical Study of Nickel Doped Chromites as Anodes for H2/CH4-fueled Solid Oxide Fuel Cells," *Applied Catalysis B: Environmental* 346 (2012): 115–116, https://doi.org/10.1016/j.apcatb.2011.12.033.

42. D. He, Y. Gong, J. Ni, and C. Ni, "A Stable Chromite Anode for SOFC With Ce/Ni Exsolution for Simultaneous Electricity Generation and CH4 Reforming," *Separation and Purification Technology* 315 (2023): 123739, https://doi.org/10.1016/j.seppur.2023.123739.

43. D.-M. Amaya-Dueñas, G. Chen, A. Weidenkaff, et al., "A-site Deficient Chromite With in Situ Ni Exsolution as a Fuel Electrode for Solid Oxide Cells (SOCs)," *Journal of Materials Chemistry A* 9 (2021): 5685–5701, https://doi.org/10.1039/D0TA07090D.

44. S. Gupta, M. K. Mahapatra, and P. Singh, "Phase transformation, thermal expansion and electrical conductivity of lanthanum chromite," *Materials Research Bulletin* 48 (2013): 3262–3267.

45. D. Jennings, M. L. Weber, A. Meise, et al., "Direct Atomic-scale Investigation of the Coarsening Mechanisms of Exsolved Catalytic Ni Nanoparticles," *Nature Communications* 16 (2025): 6830, https://doi.org/10.1038/s41467-025-61971-z.

46. J. M. Serra, V. B. Vert, M. Betz, V. A. C. Haanappel, W. A. Meulenberg, and F. Tietz, "Screening of A-Substitution in the System $A_{0.68}Sr_{0.3}Fe_{0.8}Co_{0.2}O_{3-\delta}$ for SOFC Cathodes," *Journal of the Electrochemical Society* 155 (2008): B207, https://doi.org/10.1149/1.2818766.

47. J. M. Serra, S. Uhlenbruck, W. A. Meulenberg, H. P. Buchkremer, and D. Stöver, "Nano-structuring of Solid Oxide Fuel Cells Cathodes," *Topics in Catalysis* 40 (2006): 123–131, https://iopscience.iop.org/article/10.1149/1.2818766/meta.

48. N. Schell, A. King, F. Beckmann, T. Fischer, M. Muller, and A. Schreyer in 6th International Conference on Mechanical Stress Evaluation by Neutrons and Synchrotron Radiation (MECA SENS VI 2011), (University of Hamburg, 2011): 57–61.

49. M. Storm, P. Staron, and C. Krywk, "Pydidas: a tool for automated X-ray diffraction data analysis," *Journal of Applied Crystallography* 2025, 58, 1476, https://doi.org/10.1107/S160057672500398X.

50. H. M. Rietveld, "A Profile Refinement Method for Nuclear and Magnetic Structures," *Journal of Applied Crystallography* 2 (1969): 65–71, https://doi.org/10.1107/S0021889869006558.

51. J. Rodríguez-Carvajal, "Recent Advances in Magnetic Structure Determination by Neutron Powder Diffraction," *Physica B: Condensed Matter* 192 (1993): 55–69, https://doi.org/10.1016/0921-4526(93)90108-I.

52. S. Haas, X. Sun, A. L. C. Conceição, J. Horbach, and S. Pfeffer, "The New Small-angle X-ray Scattering Beamline for Materials Research at PETRA III: SAXSMAT Beamline P62," *Journal of Synchrotron Radiation* 30 (2023): 1156–1167, https://doi.org/10.1107/S1600577523008603.

53. G. Kostorz and S. W. Lovesey, Neutron Scattering—General Introduction, in *Treatise on Materials Science & Technology*, ed. G. Kostorz, (Elsevier, 1979): 1–67.

54. I. Bressler, J. Kohlbrecher, and A. F. Thunemann, "SASfit: A Tool for Small-angle Scattering Data Analysis Using a Library of Analytical Expressions," *Journal of Applied Crystallography* 48 (2015): 1587–1598, https://doi.org/10.1107/S160057671501654.

## Supporting Information

Additional supporting information can be found online in the Supporting Information section.

**Supporting file**: admi70314-sup-0001-SuppMat.docx